PAPER

Check for updates

Preparation and characterization of doped hollow carbon spherical nanostructures with nickel and cobalt metals and their catalysis for the green synthesis of pyridopyrimidines†

Maryam Taheri, [ID] Hossein Naeimi [ID] * and Amir Hossein Ghasemi [ID]

Fused heterocyclic systems containing the pyrimidine ring structure perform a significant role in numerous biological and pharmaceutical processes. Their properties include antibacterial, antifungal, anti-fever, anti-tumor, and antihistamine. As pyridopyrimidines are important in the essential fields of pharmaceutical chemistry, efficient methods for preparing these heterocycles are presented. In this study, a method for producing improved hollow carbon sphere nanostructures with cobalt and nickel (Co-Ni@HCSs) is presented. The nanocatalyst was prepared and identified by applying Fourier-transform infrared spectroscopy (FT-IR), X-ray powder diffraction (XRD), field-emission scanning electron microscopy (FE-SEM), transmission electron microscopy (TEM), energy-dispersive X-ray spectroscopy (EDS), Brunauer–Emmett–Teller (BET), and elemental mapping techniques. The Co-Ni@HCSs nanocatalyst was proved to be highly efficient in synthesizing pyranopyrimidine derivatives. The sizeable active site, economic catalyst loading, easy workup, reusability, green reaction conditions, and excellent yields of all derivatives are some of the significant features of this process. Also, applying response surface methodology (RSM) and the Box–Behnken design (BBD) techniques allowed us to determine the influential factors of the laboratory variables and identify the optimum conditions for superior catalytic activity. Finally, synthesized organic compounds were identified by utilizing melting point, FT-IR, and hydrogen-1 nuclear magnetic resonance (^{1}H NMR) analyses.

1. Introduction

Pyridopyrimidine is an organic heterocyclic compound consisting of a pyridine ring fused orthogonally at any location to a pyrimidine ring. Pyridopyrimidines and relevant fused heterocycles are of importance as potential bioactive molecules. They have been extensively applied in medicinal,[1,2] and biological chemistry[3–5] due to the range of their available products that includes vast chemical variety and their five feasible substitution localities.[6]

Hollow nanostructures are a group of specific nanomaterials identified based on their morphologies. Hollow nanostructures can be classified into several groups. For example, some of the most common hollow nanostructures are hollow boxes, fibers, tubes, spheres, *etc.*, reflecting different overall forms.[7] Researchers have quickly discovered exciting properties related to fantastic hollow structures, such as high loading capacity, low density, and large surface area, and illustrated a vast range of applications,[8] such as nano-drug delivery systems,[9,10] catalysis,[11,12] energy storage,[13,14] sensors,[15,16] biomedicine,[17,18] and so forth.[19] The importance of hollow sphere structures in catalysis is due to their shape. Three-dimensional (3D) hollow spheres have developed as potential structures due to their high catalytic activity, large surface area, specific high porosity, ultra-low density, and adequate adsorption positions for a synthesis reaction.[20,21]

Bimetallic catalysts are significant heterogeneous catalysts due to their superior catalytic activity compared to single metal catalysis components.[22] Namely, metal particles combined with two metal ingredients present different catalytic activities to monometallic catalysts.[23] Bimetallic catalysts show a combination of the properties associated with the presence of each of the two single metals and produce unique properties due to synergetic effects among the two metals present. The synergic effect is the main advantage of bimetallic catalysts. Sometimes, depending on the metals used and on the studied reaction, the catalytic activity of the bimetallic catalyst is more potent than the total activity of the respective single metallic catalysts.[24,25] However, not all bimetallic catalysts exhibit a synergic effect.

Due to the significance of the bimetallic hollow nanostructure catalyst prepared from green materials that resulted in

Department of Organic Chemistry, Faculty of Chemistry, University of Kashan, Kashan, 87317-51167, Iran. E-mail: naeimi@kashanu.ac.ir; Fax: +983155912397; Tel: +983155912388

pyridopyrimidine, we hope to design and synthesize a nano hollow structure by a hydrothermal technique to form hollow carbon sphere nanostructures. Additionally, the influences of various experimental factors on the catalytic reaction of the synthesis of pyridopyrimidine derivatives were investigated and the reaction conditions were optimized by applying the Box–Behnken experimental design methodology to gain an excellent yield of product.

2. Experimental

2.1. Materials and apparatus

The solvents, chemical compounds, and reagents were purchased from Sigma-Aldrich, Merck, and Sinopharm Chemical Companies in high purities. The reagents were used without any further purification. The ^1H NMR spectra were recorded in DMSO-d_6 solvent using a Bruker Avance-400 MHz spectrometer in the presence of $Si(CH_3)_4$ as a chemical shift reference. The IR spectra were recorded on an FT-IR Magna 550 spectrometer using KBr plates in the range of 400–4000 cm^{-1}. Melting points were measured by Yanagimoto micro melting point equipment. A BANDELIN ultrasonic HD 3200 with probe model KE76, with a diameter of 6 mm, was used for homogenizing the reaction mixture. A Philips X'Pert Pro apparatus was used to record XRD patterns with Cu Kα radiation ($\lambda = 0.154056$ \ngström wavelengths) from 10° to 80° (2θ). Nitrogen adsorption–desorption isotherms to estimate surface areas and pore size in the nanostructure at −196 °C were recorded by a BEL-SORP-mini II. Field emission scanning electron microscopy (FE-SEM) of the nanoparticles was performed on a Zeiss which operated at a 15 kV accelerating voltage. TEM images were obtained using a Philips EM208S that operated at an acceleration of 20–100 kV.

2.2. General procedure for the preparation of the hollow carbon sphere nanocatalyst

2.2.1. General procedure for the preparation of SiO$_2$ spheres. SiO$_2$ spheres were synthesized by applying the Stöber method. For the preparation of SiO$_2$ spheres, tetraethyl orthosilicate (0.6 mL) was combined with a mixture of deionized water (23.5 mL), isopropyl alcohol (63.3 mL), and aqueous ammonia (30%, 13 mL) and powerfully stirred with a magnetic stirrer at room temperature for 80 min. Then, 6 mL of tetraethyl orthosilicate was slowly added dropwise into the solution at 40 °C for 2.5 h. Next, the suspension was centrifuged, and the SiO$_2$ spheres were collected and washed three times with deionized water and ethanol. The SiO$_2$ spheres were dried in a vacuum oven at 80 °C overnight.

2.2.2. General procedure for the preparation of Co-Ni/carbon@SiO$_2$ core–shell spheres. First, 30 mg of SiO$_2$ spheres and 30 mL of deionized water were dispersed by sonication for 30 min, and then 0.5 g of glucose, 15 mL of cobalt(II) chloride solution (1 M), and 15 mL of nickel(II) chloride solution (1 M) were added. The mixture was stirred for 15 min and then a 250 mL Teflon-lined stainless-steel autoclave was used for hydrothermal processing, and the sample was finally placed in

an electric oven at 180 °C for 24 h. The Teflon-lined stainless steel autoclave mixture was filtered, and the precipitate was washed twice with deionized water and ethanol and dried at 70 °C.

2.2.3. General procedure for the preparation of Co-Ni@HCSs. To eliminate the SiO$_2$ in the synthesized Co-Ni/carbon@SiO$_2$ core–shell spheres, they were soaked and washed in an aqueous solution of sodium hydroxide (3 M) under reflux conditions at 70 °C for 48 h, following which the Co-Ni@hollow carbon spheres (Co-Ni@HCSs) were obtained. Finally, the catalyst was separated and dried at 70 °C. A graphical depiction of the preparation of the Co-Ni@HCSs is shown in Fig. 1.

2.3. General procedure for the multicomponent synthesis of pyridopyrimidines

1 mmol of aryl aldehyde, 2 mmol of thiobarbituric acid, 1.4 mmol of ammonium acetate, 0.0125 g of Co-Ni@HCSs as a catalyst, and 15 mL of ethanol as a solvent were transferred into a round-bottomed flask. Next, the mixture was stirred by a magnetic stirrer at 72.7 °C. Throughout the reaction time, the progress was controlled by the thin-layer chromatography (TLC) technique. After the reaction was completed, the reaction mixture was cooled to room temperature, and the catalyst was isolated by filtration. The product was isolated by the recrystallization method from H$_2$O and ethanol (1 : 4 mL) to give the pure product. The pyridopyrimidine products were identified by melting points, Fourier-transform infrared spectroscopy (FT-IR), and hydrogen-1 nuclear magnetic resonance (^1H NMR) analyses.

2.3.1. Spectroscopic and physical data. 5-Phenyl-2,8-dithioxo-2,3,5,8,9,10-hexahydropyrido[2,3-d:6,5-d']dipyrimidine-4,6(1H,7H)-dione, (**4a**); cream solid; m.p.: 209–211 °C, decompose (lit. m.p. 211 °C);[26] IR (KBr): ν = 3430, 3132, 1622, 1546, 1443 cm^{-1}; ^1H NMR (400 MHz, DMSO-d_6) δ (ppm): 11.56 (s, 2H, NH), 7.19 (s, 1H, NH), 7.15 (t, J = 7.6 Hz, 2H, Ar), 7.05 (d, J = 9.8 Hz, 2H, Ar, NH), 6.98 (d, J = 7.6 Hz, 2H, Ar), 6.94 (s, 1H, NH), 5.95 (s, 1H, CH).
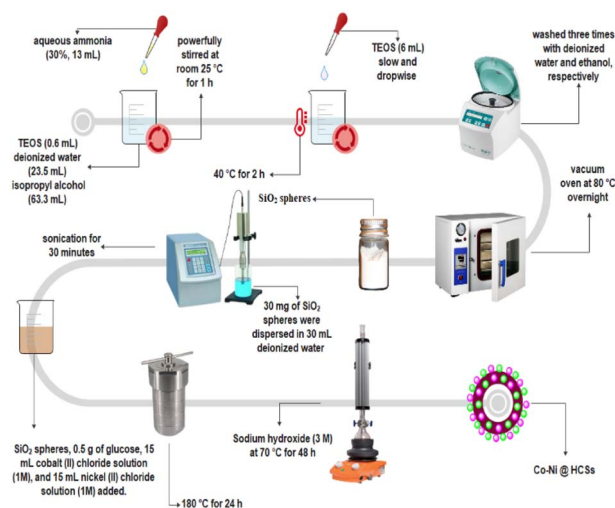

Fig. 1 Stepwise preparation of Co-Ni@HCSs.

5-(4-Nitrophenyl)-2,8-dithioxo-2,3,5,8,9,10-hexahydropyrido[2,3-d:6,5-d']dipyrimidine-4,6(1H,7H)-dione, (**4b**); light brown solid; m.p.: >300 °C, decompose (lit. m.p. 330 °C);[26] IR (KBr): $\nu =$ 3077, 1598, 1550, 1509, 1429 cm^{-1}; ^{1}H NMR (400 MHz, DMSO-d_6) δ (ppm): 11.65 (s, 2H, NH), 8.06 (d, $J =$ 8.4 Hz, 2H, Ar), 7.25 (d, $J =$ 8.4 Hz, 2H), 7.19 (s, 1H, NH), 7.06 (s, 1H, NH), 6.93 (s, 1H, NH), 6.05 (s, 1H, CH).

5-(2-Nitrophenyl)-2,8-dithioxo-2,3,5,8,9,10-hexahydropyrido[2,3-d:6,5-d']dipyrimidine-4,6(1H,7H)-dione, (**4c**); yellow solid; m.p.: 229–231 °C, decompose (lit. m.p. 230 °C);[26] IR (KBr): $\nu =$ 3487, 3195, 1614, 1542, 1426, 1358 cm^{-1}; ^{1}H NMR (400 MHz, DMSO-d_6) δ (ppm): 11.58 (s, 2H, NH), 7.51 (d, $J =$ 7.8 Hz, 1H), 7.46 (t, $J =$ 7.6 Hz, 1H), 7.31 (t, $J =$ 7.7 Hz, 1H), 7.21 (d, $J =$ 8.0 Hz, 2H, NH, Ar), 7.07 (s, 1H, NH), 6.94 (s, 1H, NH), 6.10 (s, 1H, CH).

5-(3-Fluorophenyl)-2,8-dithioxo-2,3,5,8,9,10-hexahydropyrido[2,3-d:6,5-d']dipyrimidine-4,6(1H,7H)-dione, (**4d**); white solid; m.p.: 258–260 °C, decompose; IR (KBr): $\nu =$ 3539, 3160, 1615, 1440, 1398 cm^{-1}; ^{1}H NMR (400 MHz, DMSO-d_6) δ (ppm): 11.68 (s, 1H, NH), 11.54 (s, 1H, NH), 7.20 (s, 1H, Ar), 7.20 (s, 1H, NH), 7.06 (s, 1H, NH), 6.94 (s, 1H, NH), 6.88 (t, $J =$ 8.0 Hz, 1H, Ar), 6.83 (d, $J =$ 7.7 Hz, 1H, Ar), 6.70 (d, $J =$ 11.1 Hz, 1H, Ar), 5.96 (s, 1H, CH$_3$).

5-(2-Fluorophenyl)-2,8-dithioxo-2,3,5,8,9,10-hexahydropyrido[2,3-d:6,5-d']dipyrimidine-4,6(1H,7H)-dione, (**4e**); white solid; m.p.: 240–241 °C, decompose (lit. m.p. 240 °C);[26] IR (KBr): $\nu =$ 3127, 1609, 1550, 1480 cm^{-1}; ^{1}H NMR (400 MHz, DMSO-d_6) δ (ppm): 11.66 (s, 1H, NH), 11.51 (s, 1H, NH), 7.11 (m, 4H), 6.99 (t, $J =$ 8.0 Hz, 2H), 6.93 (d, $J =$ 9.3 Hz, 1H), 6.01 (s, 1H, CH).

5-(4-Chlorophenyl)-2,8-dithioxo-2,3,5,8,9,10-hexahydropyrido[2,3-d:6,5-d']dipyrimidine-4,6(1H,7H)-dione, (**4f**); yellow solid; m.p.: 253–255 °C, decompose (lit. m.p. 257 °C);[26] IR (KBr): $\nu =$ 3117, 2885, 1625, 1562, 1520, 1442 cm^{-1}; ^{1}H NMR (400 MHz, DMSO-d_6) δ (ppm): 11.61 (s, 1H, NH), 11.55 (s, 1H, NH), 7.20 (d, $J =$ 8.7 Hz, 2H, Ar), 7.19 (s, 1H, NH), 7.06 (s, 1H, NH), 6.99 (d, $J =$ 8.1 Hz, 2H, Ar), 6.93 (s, 1H, NH), 5.93 (s, 1H, CH).

5-(3-Chlorophenyl)-2,8-dithioxo-2,3,5,8,9,10-hexahydropyrido[2,3-d:6,5-d']dipyrimidine-4,6(1H,7H)-dione, (**4g**); white solid; m.p.: 253–255 °C, decompose; IR (KBr): $\nu =$ 3106, 2885, 1666, 1620, 1520, 1546, 1435 cm^{-1}; ^{1}H NMR (400 MHz, DMSO-d_6) δ (ppm): 11.65 (s, 1H, NH), 11.53 (s, 1H, NH), 7.19 (t, $J =$ 3.9 Hz, 2H), 7.12 (d, $J =$ 8.0 Hz, 1H), 7.06 (s, 1H), 6.95 (d, $J =$ 12.3 Hz, 3H), 5.96 (s, 1H, CH).

5-(3-Bromophenyl)-2,8-dithioxo-2,3,5,8,9,10-hexahydropyrido[2,3-d:6,5-d']dipyrimidine-4,6(1H,7H)-dione, (**4h**); white solid; m.p.: 245–246 °C, decompose (lit. m.p. 246–248 °C);[27] IR (KBr): $\nu =$ 3111, 1619, 1547, 1434 cm^{-1}; ^{1}H NMR (400 MHz, DMSO-d_6) δ (ppm): 11.70 (s, 1H, NH), 11.57 (s, 1H, NH), 7.26 (d, $J =$ 8.1 Hz, 1H, Ar), 7.19 (s, 1H, Ar), 7.14 (t, $J =$ 8.0 Hz, 1H, Ar), 7.07 (s, 2H, CH, Ar, NH), 6.99 (d, $J =$ 8.1 Hz, 1H, Ar), 6.94 (s, 1H, NH), 5.96 (s, 1H, CH).

5-(4-Bromophenyl)-2,8-dithioxo-2,3,5,8,9,10-hexahydropyrido[2,3-d:6,5-d']dipyrimidine-4,6(1H,7H)-dione, (**4i**); white solid; m.p.: 379–381 °C, decompose (lit. m.p. 380 °C);[28] IR (KBr): $\nu =$ 3325, 3081, 1594, 1533, 1486 cm^{-1}; ^{1}H NMR (400 MHz, DMSO-d_6) δ (ppm): 11.65 (s, 1H, NH), 11.54 (s, 1H, NH), 7.33 (d, $J =$ 8.2 Hz, 2H, Ar), 7.19 (s, 1H, NH), 7.06 (s, 1H, NH), 6.94 (d, $J =$ 4.3 Hz, 2H, Ar), 6.93 (s, 1H, NH), 5.90 (s, 1H, CH).

2,8-Dithioxo-5-(p-tolyl)-2,3,5,8,9,10-hexahydropyrido[2,3-d:6,5-d']dipyrimidine-4,6(1H,7H)-dione, (**4j**); white solid; m.p.: 199–201 °C, decompose (lit. m.p. 198–200 °C);[29] IR (KBr): $\nu =$ 3185, 3064, 2906, 1653, 1594, 1594, 1534, 1422 cm^{-1}; ^{1}H NMR (400 MHz, DMSO-d_6) δ (ppm): 11.61 (s, 1H, NH), 11.48 (s, 1H, NH), 7.20 (s, 1H, NH), 7.07 (s, 1H, NH), 6.95 (d, $J =$ 7.2 Hz, 3H, Ar, NH), 6.86 (d, $J =$ 7.6 Hz, 2H, Ar), 5.90 (s, 1H, CH), 2.20 (s, 3H, Me).

5-(4-Methoxyphenyl)-2,8-dithioxo-2,3,5,8,9,10-hexahydropyrido[2,3-d:6,5-d']dipyrimidine-4,6(1H,7H)-dione, (**4k**); orange solid; m.p.: 277–278 °C, decompose (lit. m.p. 277–279 °C);[27] IR (KBr): $\nu =$ 3068, 2899, 1650, 1595, 1521, 1431 cm^{-1}; ^{1}H NMR (400 MHz, DMSO-d_6) δ (ppm): 11.60 (s, 1H, NH), 11.47 (s, 1H, NH), 7.08 (s, 3H, NH), 6.88 (d, $J =$ 8.3 Hz, 2H, Ar), 6.72 (d, $J =$ 8.2 Hz, 2H, Ar), 5.89 (s, 1H, CH), 3.66 (s, 3H, OMe).

5-(3-Methoxyphenyl)-2,8-dithioxo-2,3,5,8,9,10-hexahydropyrido[2,3-d:6,5-d']dipyrimidine-4,6(1H,7H)-dione, (**4l**); orange solid; m.p.: 240–242 °C, decompose (lit. m.p. 242 °C);[30] IR (KBr): $\nu =$ 3155, 1605, 1537, 1437 cm^{-1}; ^{1}H NMR (400 MHz, DMSO-d_6) δ (ppm): 11.35 (s, 2H, NH), 7.05 (m, 5H), 6.75 (m, 2H), 5.89 (s, 1H, CH), 3.59 (s, 3H, Me).

2.4. Design of the experiments and response surface methodology (RSM)

The response surface methodology was applied to optimize and improve the reaction conditions and product yield based on a Box–Behnken design (BBD) technique for the catalytic performance of the Co-Ni@HCSs nanocatalyst for the synthesis of pyridopyrimidine derivatives. The ranges and levels of the factors based on the Box–Behnken design technique are displayed in Table 1. Three factors of catalyst dose (A), temperature (B), and time of the reaction (C) at three levels (low level, central point, and high level) were chosen as the variables.

The Design-Expert software (ver.13.0.5) was applied to design experiments and analyses of the experimental data. The number of experiments was determined by the Box–Behnken design method based on the following equation:[31]

Table 1 Experimental ranges and three levels of the independent variables

Variable	Factor	Range and level		
		Low level (−1)	Central point (0)	High level (+1)
Catalyst dose (mg)	A	5	12.50	20
Temperature (°C)	B	25	52.50	80
Time of reaction (min)	C	5	15	25

$$N = 2k(k - 1) + C_0 \qquad (1)$$

In eqn (1), k is the number of factors, and C_0 is the replicate number of the central point. According to eqn (1), three factors and five central points are considered, so there was a total of 17 runs. The Box–Behnken experimental design model equation can be matched to a second-order polynomial model. RMS gives the second-order polynomial model that was applied to show the interactive effects between the experimental variables to optimize the reaction conditions and predict the yield of the product. The quadratic equation model can be expressed:[32]

$$Y = \beta_0 + \beta_1 A + \beta_2 B + \beta_3 C + \beta_4 AB + \beta_5 AC + \beta_6 BC + \beta_7 A^2 + \beta_8 B^2 + \beta_9 C^2 + \varepsilon \qquad (2)$$

In eqn (2), Y is the predicted response (% product yield), β_0 is the zero-order constant, which denotes the regression coefficients representing the offset term, β_{1-a} is the main effect, β_{4-6} is the interaction effect, β_{7-9} is the quadratic effect, and the random error is ε.

3. Results and discussion

3.1. Preparation and characterization of the Co-Ni@HCS nanocatalyst

The Co-Ni@HCSs are prepared in three steps, as shown in Fig. 2. In the first step, SiO$_2$ spheres were prepared from tetraethyl orthosilicate with the Stöber method.[33] Then, the SiO$_2$ spheres were coated with glucose, cobalt, and nickel through the hydrothermal method. Finally, the Co-Ni@HCSs were prepared by etching SiO$_2$ spheres with concentrated sodium hydroxide.

After the preparation of the Co-Ni@HCSs, the nanocatalyst was identified by different analyses such as XRD, FT-IR, FE-SEM, TEM, EDS, elemental mapping, and BET techniques. The X-ray diffraction patterns of the SiO$_2$ spheres (Fig. 3a) and Co-Ni@HCSs (Fig. 3b) were studied. Fig. 3a illustrates a broad signal corresponding to the amorphous nature of the SiO$_2$ spheres,[34] and Fig. 3b is due to XRD patterns of the Co-Ni@HCSs. No specific signal of cobalt and nickel was observed in the XRD pattern of the Co-Ni@HCSs due to the prepared hollow spheres having amorphous morphology.

The FT-IR spectra of the SiO$_2$ spheres (a), Co-Ni/SiO$_2$@carbon core–shell spheres (b), and Co-Ni@HCSs are shown in Fig. 4. For the SiO$_2$ spheres (Fig. 4a), the peak at about 953 cm^{-1} is due to the stretching vibration of the Si–OH bond. The peaks at 472 cm^{-1} and 800 cm^{-1} correspond to bending vibrations of
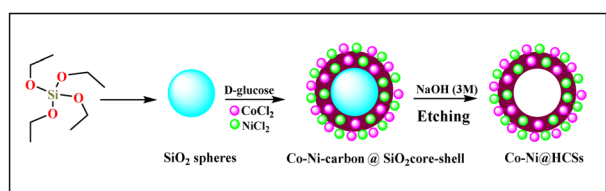
the Si–O–Si bonds. The signal that appears at 1030 cm^{-1} corresponds to the stretching vibration of the Si–O–Si bonds. The signal at 1375 cm^{-1} is due to the stretching vibration of the aliphatic C–H bonds. Finally, the absorption peaks at 1633 and 3421 cm^{-1} are due to the O–H bond's bending and stretching vibrations.

In the FT-IR spectrum of the Co-Ni/SiO$_2$@carbon core–shell spheres (Fig. 4b), the peak at 1622 cm^{-1} was assigned to the vibration of C=O due to the glucose structure. The spectrum shows some peaks at 1000–1400 cm^{-1} corresponding to the OH and C–O bonds. Additionally, the signal at 3427 cm^{-1} is due to the O–H bond on the surface of the carbon spheres.

In the spectrum of the Co-Ni@HCSs (Fig. 4c), the absorption peak at 1621 cm^{-1} is due to C=O, and the broad peak at 3426 cm^{-1} is due to the O–H bond. No peaks corresponding to Si–O–Si or Si–OH were observed, which indicates the successful removal of the silicon and eventually the formation of hollow spheres.

The scanning electron microscopy (FE-SEM) and transmission electron microscopy (TEM) images of the Co-Ni@HCSs are displayed in Fig. 5. The spherical morphology of the Co-Ni@HCSs nanocatalyst is easily identifiable in the SEM images (Fig. 5a and b). The average size of the hollow spheres is 400 nm, but the size of the cobalt and nickel nanoparticles stabilized on the surface of the hollow spheres is identified to be less than 30 nm.
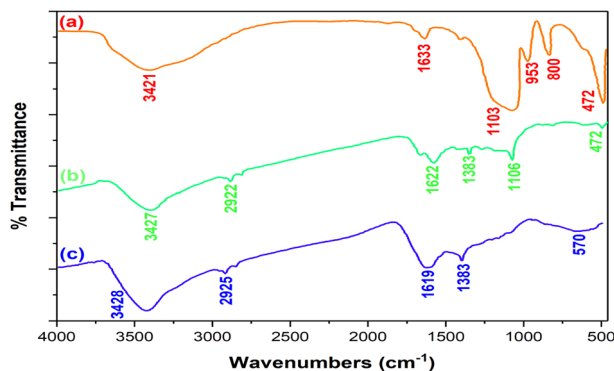

Fig. 3 XRD patterns: (a) SiO$_2$ spheres, (b) Co-Ni@HCSs.

Fig. 2 Preparation of the Co-Ni@HCSs nanocatalyst.

Fig. 4 Comparison of the FT-IR spectra of SiO$_2$ spheres (a), Co-Ni/SiO$_2$@carbon core–shell spheres (b), and Co-Ni@HCSs (c).
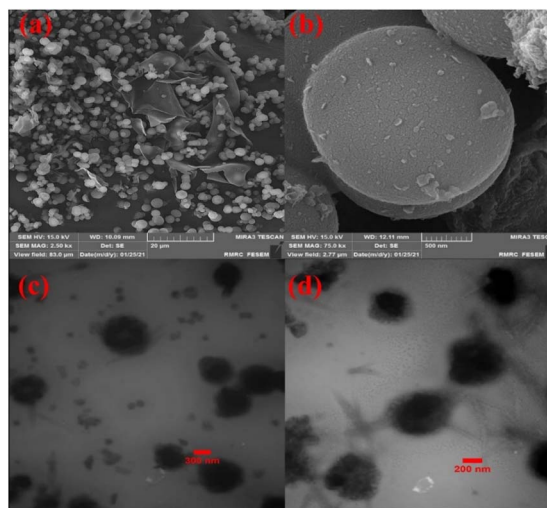
Fig. 5 FE-SEM images of the Co-Ni@HCSs (a and b); TEM images of the Co-Ni@HCSs (c and d).

Additionally, the TEM images (Fig. 5c and d) of the nanoparticles show the formation of the hollow spheres' nanostructure.

The elemental energy-dispersive X-ray (EDS) spectrum of the Co-Ni@HCSs nanocatalyst was investigated (Fig. 6). The EDS spectrum shows that the main elements in this fabricated nanocatalyst are carbon, cobalt, and nickel.

To determine the amount of Co and Ni in the catalyst structure, inductively coupled plasma atomic emission spectroscopy (ICP-OES) was used. The results showed 1.37×10^{-4} mol g^{-1} of Ni and 1.21×10^{-4} mol g^{-1} of Co were loaded on the Co-Ni@HCSs nanocatalyst.

The energy-dispersive X-ray spectroscopy elemental mapping pictures of the Co-Ni@HCSs nanocatalyst are displayed in Fig. 7. As shown in Fig. 7, the cobalt and nickel nanoparticles are evenly distributed throughout the catalyst surface. The homogeneous distribution of cobalt and nickel nanoparticles increased the efficiency and increased the effective contact surface of the nanocatalyst. The homogeneous distribution of metal nanoparticles throughout the carbon spheres results in a similar catalyst effect throughout the catalyst surface. In addition, the homogeneous dispersion of the nanoparticles
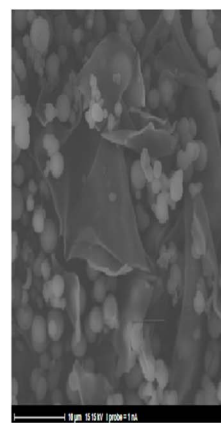

Fig. 7 EDS elemental mapping pictures of the Co-Ni@HCSs nanocatalyst.
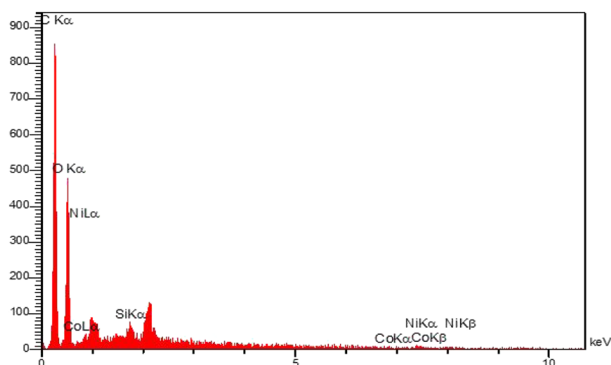
creates a synergetic effect between the metals and the raw reaction material, which leads to an increase in the catalyst efficiency.

The Brunauer–Emmett–Teller (BET) technique was used to estimate the surface area, pore volume, and pore size of Co-Ni@HCSs nanocatalyst (Fig. 8). The surface area is 240.99 m^2 g^{-1}, and the total pore volume (P/P_0) is 1.0181 cm^3 g^{-1} (Fig. 8a and b). The average pore diameter is 16.899 nm. Based on the Barrett–Joyner–Halenda (BJH) method, Fig. 8c shows the pore size and pore volume distribution. These results indicate a high contact surface of the hollow spheres, and as a result, increasing
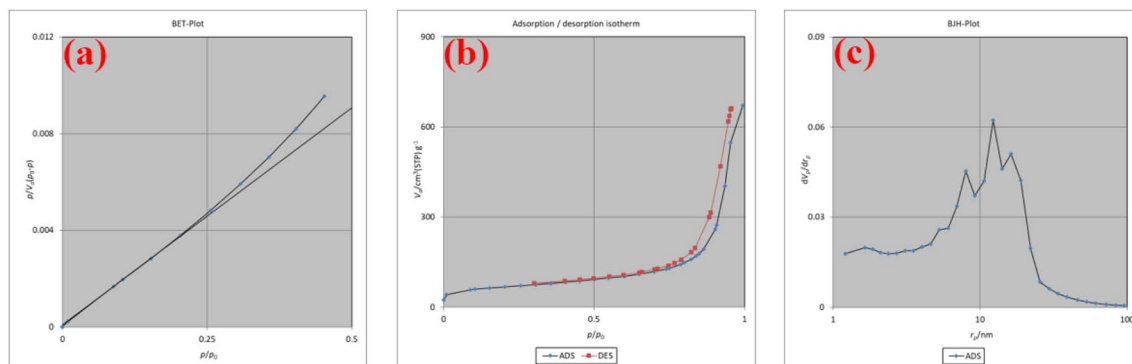

Fig. 6 EDS spectrum of the Co-Ni@HCSs nanocatalyst.

Fig. 8 The BET plot (a), adsorption/desorption isotherm (b), and BJH plot (c) of the Co-Ni@HCSs nanocatalyst.
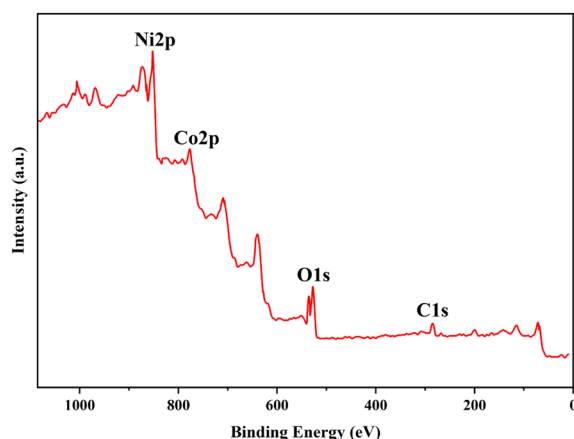

Fig. 9 X-ray photoelectron spectrum of the Co-Ni@HCSs.

the catalyst contact surface improves the catalyst efficiency and reduces the reaction time.

The X-ray photoelectron spectrum (XPS) of the Co-Ni@HCSs is shown in Fig. 9. The hollow carbon sphere nanostructures with cobalt and nickel were subjected to XPS measurements to obtain more detailed information about their elemental composition. As can be seen from the XPS spectrum, the catalyst structure contains elements such as carbon, oxygen, cobalt, and nickel. The C 1s region at 286.3 eV is generally associated with the sp^2 carbon–carbon double bond or sp^3 carbon–carbon single bond, as shown in Fig. 9. The O 1s XPS spectrum showed two peaks with binding energies at 527.3 and 532.6 eV, which are related to Ni–O and Ni–OH, respectively. A Co 2p XPS spectrum revealed two main peaks corresponding to the Co $2p_{3/2}$ and Co $2p_{1/2}$ energy levels, with binding energies of 783.0 and 797.9 eV. Based on the XPS spectrum of Ni 2p in this figure, peaks at binding energies of 858.6 eV and 854.2 eV were attributed to Ni $2p_{3/2}$, and 875.6 eV and 871.4 eV to Ni $2p_{1/2}$. The

Table 2 Results of the analyses of variance for the Co-Ni@HCSs nanocatalyst

Run	Factor A A: catalyst dose (mg)	Factor B B: temperature (°C)	Factor C C: time (min)	The yield of product (%) in EtOH Experimental[a] (%)	Predicted (%)
1	12.5	52.5	15	91	89.80
2	20	80	15	97	97.88
3	12.5	25	5	35	35.13
4	5	25	15	13	12.13
5	12.5	25	25	67	65.88
6	12.5	80	5	93	94.13
7	12.5	52.5	15	91	89.80
8	12.5	52.5	15	89	89.80
9	12.5	80	25	97	96.88
10	5	80	15	64	62.13
11	20	52.5	25	78	77.25
12	12.5	52.5	15	88	89.80
13	20	52.5	5	68	66.00
14	5	52.5	25	40	42.00
15	20	25	15	56	57.88
16	12.5	52.5	15	90	89.80
17	5	52.5	5	19	19.75

[a] Isolated yield.

XPS spectrum clearly indicates the presence of Co^{2+} and Ni^{2+} in the catalyst structure.

3.2. Results of the statistical analysis of the process and product optimization

The response surface methodology and the Box–Behnken design method were utilized to determine the interactive effects of the experimental variables for finding the optimum conditions for the reactions. Primarily, the reaction of 2-nitrobenzaldehyde (1 mmol), thiobarbituric acid (2 mmol), and ammonium acetate (1.4 mmol) was chosen as a model reaction. To determine the optimum experimental conditions, the catalyst activity was investigated with a variety of factors, including temperature, time of the reaction, and catalyst dose in three solvents (EtOH, H_2O, and EtOH/H_2O). Based on laboratory data and calculations, the best reaction solvent was ethanol. To avoid increasing the computational data provided, calculations related to the ethanol solvent are included in the article, and the

tables and graphs obtained from the other solvents (H_2O and EtOH/H_2O) are given in the ESI of the article (Fig. S28, S29, and Tables S1–S3, ESI†).

Following the experimental ranges and three levels of the independent variables (Table 1), calculated outcomes from the Box–Behnken quadratic model are summarized in Table 2.

The quadratic model to predict the percentage product yield of the model reaction with the Co-Ni@HCSs nanocatalyst in ethanol as a solvent is shown in the following equation:

$$Y = 89.8 + 20.375A + 22.5B + 8.375C - 2.5AB - 2.75AC - 7BC - 27.025A^2 - 5.275B^2 - 11.525C^2 \quad (3)$$

where the factors A, B, and C represent the aforementioned independent variables (Table 1), and Y is the percentage product yield. According to Fig. 10, the predicted results are close to the experimental (actual) results, and the calculations are very accurate. The correlation coefficient square (R^2) value of 0.997 and an adjusted correlation coefficient (R^2_{adj}) of 0.994, and a correlation predicted coefficient square (R^2_{pre}) of 0.972 indicate high reliability. Additionally, the Adeq. model precision of 56.875 (which is much higher than 4.0) indicates an adequate signal.

The standard analysis of variance (ANOVA) of the quadratic model is shown in Table 3, and the fitting quality was verified by ANOVA. In Table 3, the probability (P-value) is applied as a measure for evaluating the significance of the variables. A P-value smaller than 0.0500 shows that the model terms are significant. As a result, the A (catalyst dose), B (temperature), C (time), A^2, B^2, C^2, and BC (temperature × time) factors, with P-values smaller than 0.0500, were the highly significant factors in the increase of catalytic activity and the reaction yield in ethanol. The AB (catalyst dose × temperature) and AC (catalyst dose × time) factors had lower significance than the previous factors; however, they were effective in the reaction yield due to the low P-value. The Box–Behnken design (BBD) technique and the predicted model show 3D response surface plots and corresponding contour plots in Fig. 11. The interaction influence
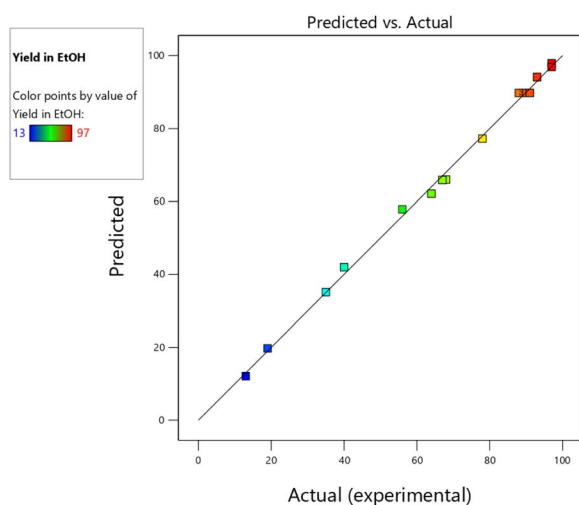

Fig. 10 The predicted *vs.* actual (experimental) product yield of the model reaction with the Co-Ni@HCSs nanocatalyst in ethanol.

Table 3 The ANOVA results of the quadratic model

Source	Sum of squares	DF[a]	Mean square	F-value	P-value	Significance[b]
Model	12 199.42	9	1355.49	350.77	<0.0001	**
A – catalyst dose	3321.13	1	3321.13	859.44	<0.0001	**
B – temperature	4050.00	1	4050.00	1048.06	<0.0001	**
C – time	561.13	1	561.13	145.21	<0.0001	**
AB	25.00	1	25.00	6.47	0.0385	*
AC	30.25	1	30.25	7.83	0.0266	*
BC	196.00	1	196.00	50.72	0.0002	**
A^2	3075.16	1	3075.16	795.79	<0.0001	**
B^2	117.16	1	117.16	30.32	0.0009	**
C^2	559.27	1	559.27	144.73	<0.0001	**
Residual	27.05	7	3.86			
Lack of fit	20.25	3	6.75	3.97	0.1080	
Pure error	6.80	4	1.70			
Cor. total	12 226.47	16				

[a] Degree of freedom. [b] *Represents significant, **represents highly significant.
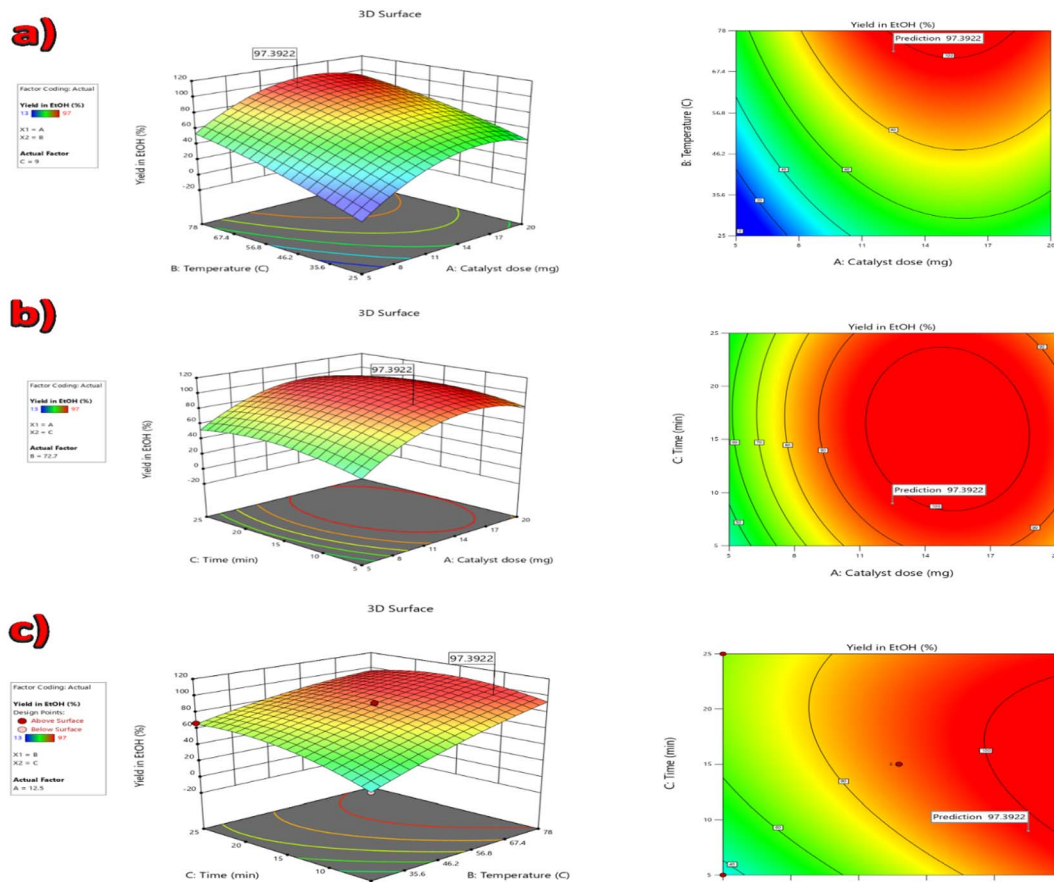
Fig. 11 The 3D response surface plots and their corresponding contour plots: (a) interactive effect of catalyst dose and temperature, (b) interactive effect of catalyst dose and time, (c) interactive effect of temperature and time.

among any pair of two experimental variables and their level (Table 1) is plotted in Fig. 11. All of the factors are significant in the yield of the product.

Based on the response surface methodology outcomes achieved from all 15 experimental runs, the optimal reaction conditions for the catalytic performance of the Co-Ni@HCSs nanocatalyst for the model reaction synthesis are as follows: A

$= 12.50$ mg (catalyst dose), $B = 72.7$ °C (temperature), $C = 9$ min (time), and the predicted yield of the product is 97.39%. Four reactions were performed under the predicted conditions to ensure the validity of the predicted model and the optimal reaction conditions. An average product yield of 9.37% was obtained, in good accordance with the predicted model.

The synergistic effect of the Co-Ni@HCSs nanocatalyst was investigated, and the results are shown in Fig. 12. Four catalysts, hollow carbon spheres, Co@HCSs, Ni@HCSs, and Co-Ni@HCSs, were used in the model reaction, and the efficiency of each catalyst was obtained. As shown in Fig. 12, the hollow carbon spheres did not show any catalytic activity. The Co@HCSs nanocatalysts showed higher efficiency than the Ni@HCSs nanocatalysts. When two nanoparticles of cobalt and nickel participated together (Co-Ni@HCSs) in the reaction as a catalyst, we observed a synergistic effect, resulting in a significant increase in the percentage of products and a decrease in the reaction time.

After optimizing the reaction conditions with numerous solvents, catalyst dose, time of reaction, and temperature, the synthesis of pyridopyrimidine derivatives was performed using thiobarbituric acid, ammonium acetate, and the different aryl aldehydes. The results of the catalytic reaction are displayed in Table 4.
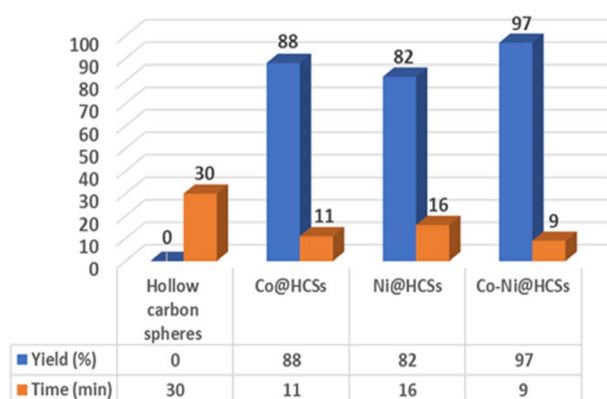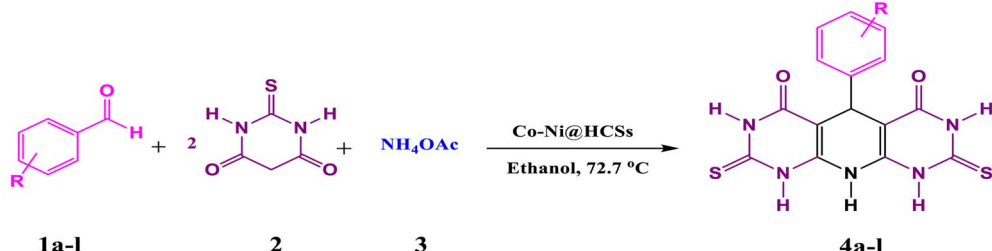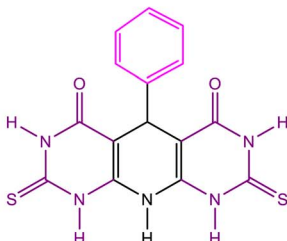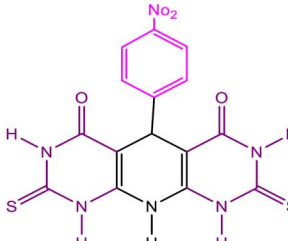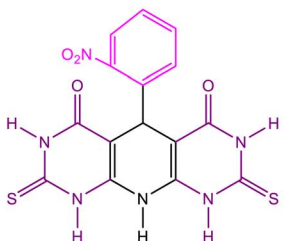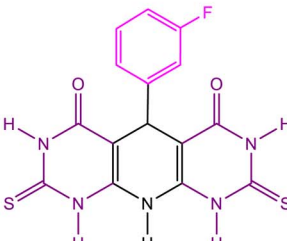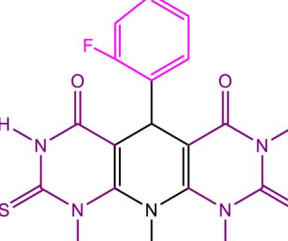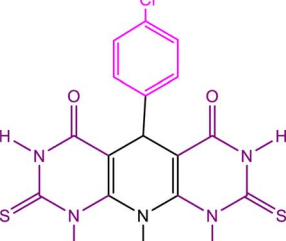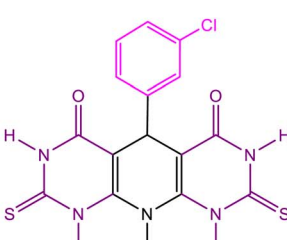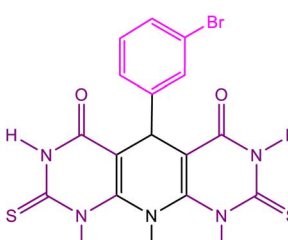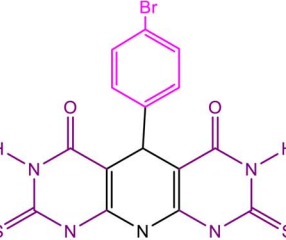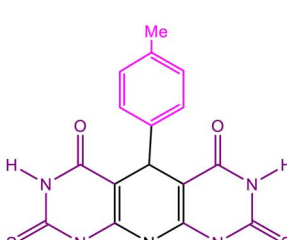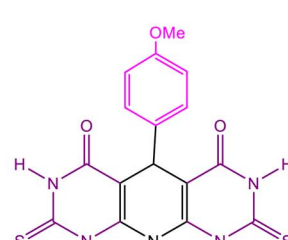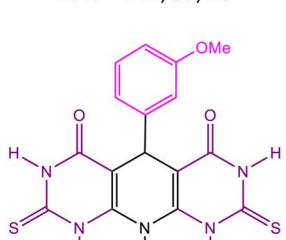

Fig. 12 Comparison of the catalytic effects between hollow carbon spheres, Co@HCSs, Ni@HCSs, and Co-Ni@HCSs for the synthesis of **4c**.

Table 4 Synthesis of pyridopyrimidine derivatives

| 1a-l | 2 | 3 | 4a-l |

4a-l[a], yield[b] (%), time (min)

4a: R = H, 93, 14

4b: R = 4-NO$_2$, 96, 6

4c[c]: R = 2-NO$_2$, 97, 9

4d: R = 3-F, 92, 16

4e: R = 2-F, 96, 15

4f: R = 4-Cl, 97, 10

4g: R = 3-Cl, 92, 10

4h: R = 3-Br, 96, 14

4i: R = 4-Br, 97, 16

4j: R = 4-Me, 95, 20

4k: R = 4-OMe, 91, 24

4l: R = 3-OMe, 89, 20

[a] Reaction conditions: aryl aldehyde (1 mmol), thiobarbituric acid (2 mmol), ammonium acetate (1.4 mmol), Co-Ni@HCSs (0.0125 g), and 15 mL ethanol as solvent at 72.7 °C. [b] Isolated yield. [c] Model reaction.

Table 5 Comparison of the catalytic activity of the Co-Ni@HCSs nanocatalyst with the other reported catalysts for the synthesis of **4c**

Entry	Catalyst (conditions)	Time (min)	Yield[a] (%)	Ref.
1	Nano-[DMSPDE][Cl] (0.02 g, solvent-free, 110 °C)	10	88	30
2	Nano CuFe$_2$O$_4$ (10 mol%, H$_2$O, US 40 W)	12	95	35
3	CuFe$_2$O$_4$ nanoparticles (10 mol%, H$_2$O, microwave 100 W)	2	95	36
4	**Co-Ni@HCSs (0.0125 g, ethanol, 72.7 °C)**	**9**	**97**	**This work**

[a] Isolated yield.

This study applied aryl aldehyde with electron-donating and electron-withdrawing substituents to synthesize pyridopyrimidine derivatives. The product yields were excellent, and the reaction times were short. Additionally, in the aryl aldehydes with electron-withdrawing substituents, the reaction times were shorter than in the aryl aldehydes with electron-donating ones.

To compare the catalytic performance of the Co-Ni@HCSs nanocatalyst with the previously published catalysts for the synthesis of pyridopyrimidine derivatives, the model reaction was investigated, and the outcomes are displayed in Table 5.

As displayed in Table 5, the Co-Ni@HCSs nanocatalyst showed better catalytic activity than the reported catalysts. The synergistic effects due to the utilization of two metal nanoparticles and the high contact surface due to the hollow structure of the Co-Ni@HCSs nanocatalyst improved the catalytic activity of the catalyst (entry 4 *vs.* entries 1–3, Table 5).

3.3. Proposed reaction mechanism

An acceptable mechanism for the formation of pyridopyrimidine derivatives is proposed[35] in Scheme 1. The results show that the reaction occurs on the surface and inner surfaces of the hollow spheres. Initially, the CO-Ni@HCSs nanocatalyst acts as a Lewis acid due to the presence of an empty orbital and chelates with the carbonyl group of aldehyde **1**. Due to the positive oxygen charge of the carbonyl group, favorable conditions are provided for a nucleophilic attack. The activated aldehyde **1** can be first condensed with 2-thiobarbituric acid **2** to afford heterodiene **3**. This step was considered a quick Knoevenagel condensation reaction. Next, compound **3** is attacked by a Michael-type addition with extra 2-thiobarbituric acid that reacts with NH$_4$OAc **4** and tautomerization occurs to synthesize intermediate **5**. Then, the Co-Ni@HCSs nanocatalyst activates the carbonyl group of the intermediate **5**. The attack of the amine group on the carbonyl group of intermediate **5** is enhanced by the Co-Ni@HCSs nanocatalyst, and finally, the cyclization of intermediate **5** occurs. After the cyclization and synthesis of the pyridopyrimidine derivatives, the Co-Ni@HCSs nanocatalyst starts a new catalytic cycle.[30]

The active sites of the catalyst are shown in Fig. 13. According to the shape and hollow structure of the catalyst, the reaction can take place on the surface, inside the spheres, and inside the channels. The high contact surface of the catalyst
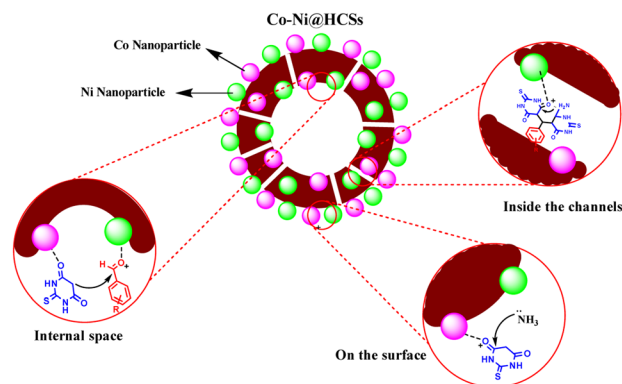
Fig. 13 The active sites of the Co-Ni@HCSs nanocatalyst.
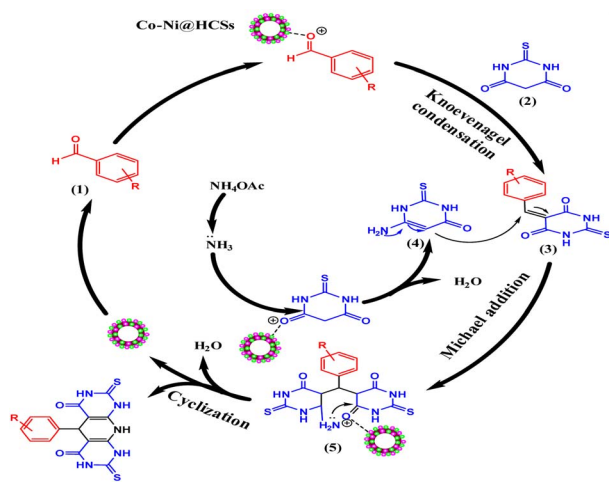
Scheme 1 Proposed reaction mechanism for the synthesis of pyridopyrimidine derivatives.
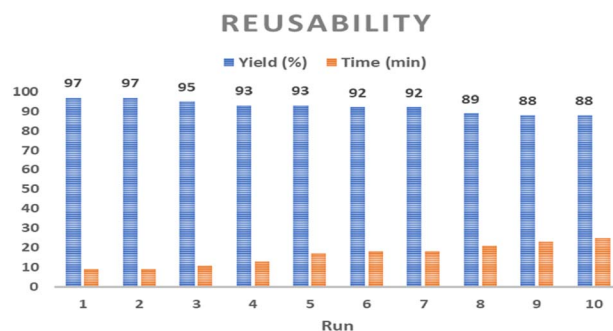
Fig. 14 The reusability of the Co-Ni@HCSs nanocatalyst under optimized reaction conditions.
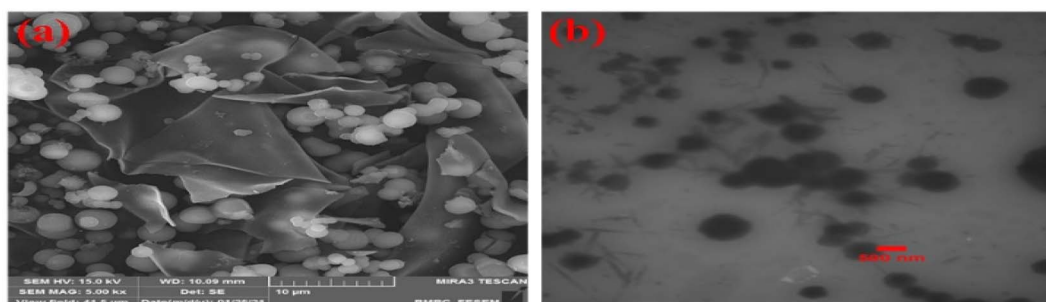
Fig. 15 FE-SEM image (a) and TEM image (b) of the Co-Ni@HCSs after recycling.

increases the efficiency and reduces the reaction time. As a result, the amount of catalyst needed to carry out the reaction is also reduced.

3.4. Reusability. One of the most important factors in designing catalysts is their reusability. Reusable catalysts have received a great deal of attention due to the importance of environmental and economic issues. In this research, the reusability of the Co-Ni@HCSs nanocatalyst was studied by reactions with thiobarbituric acid (2 mmol), 2-nitrobenzaldehyde (1 mmol), and ammonium acetate (1.4 mmol) under optimized reaction conditions to synthesize **4c**. The reaction mixture was filtered and the Co-Ni@HCSs nanocatalyst separated. Then, the filtered Co-Ni@HCSs nanocatalyst was washed with acetone and water to remove any organic compounds and salts. Finally, the catalyst was dried at 70 °C. The results of the catalyst reusability tests were shown after 10 runs (Fig. 14). After 10 runs of use of the Co-Ni@HCSs nanocatalyst, no significant decrease in catalytic activity was observed.

The leaching of the Co-Ni@HCSs nanocatalyst was also studied with the hot filtration method. The reaction of 2-nitrobenzaldehyde, thiobarbituric acid, and ammonium acetate in the presence of the Co-Ni@HCSs nanocatalyst was stopped after 4.5 min, and then the nanocatalyst was separated by a paper filter from the reaction mixture. Next, the filtrate mixture was heated, and the progress of the reaction was monitored by the thin-layer chromatography technique. The monitored reaction did not progress after filtration, so the hot filtration analysis shows that Co-Ni@HCSs nanocatalyst leaching does not happen.

According to the FE-SEM image (Fig. 15a) and TEM image (Fig. 15b) of the Co-Ni@HCSs after 6 runs of recycling, no significant changes were observed in the structure and morphology of the catalyst. The morphological and structural stability of the catalyst after several recovery steps indicates its excellent stability and the maintenance of catalytic activity under the reaction conditions.

4. Conclusion

The basic purpose of this research was to design, prepare, and characterize economical, green, and high-performance nanocatalysts. In this study, hollow spherical structures that had a high contact surface were prepared using the hydrothermal method. The use of two metal nanoparticles caused a synergistic effect on the activity of the catalyst. The presence of the two factors of high contact surface and synergistic properties in the catalyst significantly increased the reaction efficiency and reduced the reaction time. Another essential feature of the synthesized nanocatalyst was the recovery and reuse of the catalyst with minimal reduction in performance. In this research, a catalyst was designed to synthesize pyridopyrimidine derivatives. The yield of the obtained products was excellent compared to the previous reports, and the reaction time was also short. The reaction conditions were optimized using the Box–Behnken design, which gave outcomes very close to the experimental results.

Conflicts of interest

There are no conflicts to declare.

References

1 A. Rifati-Nixha, M. Arslan, N. Gençer, K. Çıkrıkıçı, B. Gökçe and O. Arslan, *J. Biochem. Mol. Toxicol.*, 2019, **33**(6), 1–6.
2 S. R. Dasari, S. Tondepu, L. R. Vadali and N. Seelam, *Synth. Commun.*, 2020, 1–12.
3 R. B. Bakr and N. A. A. Elkanzi, *J. Heterocycl. Chem.*, 2020, **57**, 2977–2989.
4 P. P. Mohire, D. R. Chandam, A. A. Patravale, P. Choudhari, V. Karande, J. S. Ghosh and M. B. Deshmukh, *Polycyclic Aromat. Compd.*, 2020, 1–19.
5 N. Kahriman, K. Peker, V. Serdaroğlu, A. Aydın, A. Usta, S. Fandaklı and N. Yaylı, *Bioorg. Chem.*, 2020, **99**, 103805.
6 F. Buron, J. Y. Mérour, M. Akssira, G. Guillaumet and S. Routier, *Eur. J. Med. Chem.*, 2015, **95**, 76–95.
7 X. Wang, J. Feng, Y. Bai, Q. Zhang and Y. Yin, *Chem. Rev.*, 2016, **116**, 10983–11060.
8 N. Yan, *Catal. Today*, 2016, **278**, 185–186.

9 M. Zhu, J. Tang, W. Wei and S. Li, *Mater. Chem. Front.*, 2020, **4**, 1105–1149.

10 C. Zhang, D. Li, P. Pei, W. Wang, B. Chen, Z. Chu, Z. Zha, X. Yang, J. Wang and H. Qian, *Biomaterials*, 2020, **237**, 119835.

11 J. Sun, Z. Dong, X. Sun, P. Li, F. Zhang, W. Hu, H. Yang, H. Wang and R. Li, *J. Mol. Catal. A: Chem.*, 2013, **367**, 46–51.

12 S. Mohammadi and H. Naeimi, *Appl. Catal., A*, 2020, **602**, 117720.

13 X.-Y. Yu, L. Yu and X. W. D. Lou, *Adv. Energy Mater.*, 2016, **6**, 1501333.

14 J. Wang, Y. Cui and D. Wang, *Adv. Mater.*, 2019, **31**, 1801993.

15 J. E. Lee, C. K. Lim, H. J. Park, H. Song, S.-Y. Choi and D.-S. Lee, *ACS Appl. Mater. Interfaces*, 2020, **12**, 35688–35697.

16 Z. Lou, Y. Wang, Y. Yang, Y. Wang, C. Qin, R. Liang, X. Chen, Z. Ye and L. Zhu, *Nanomaterials*, 2020, **10**, 378.

17 H. Tang, Y. Zheng and Y. Chen, *Adv. Mater.*, 2017, **29**, 1604105.

18 T. S. Atabaev and N. H. Hong, in *Nano-Sized Multifunctional Materials*, Elsevier, 2019, pp. 73–88.

19 J. W. Han, F. Hollmann, R. Luque, I. K. Song, G. Talarico, T. Tatsumi and N. Yan, *Mol. Catal.*, 2022, **522**, 112233.

20 D. V. Shinde, L. De Trizio, Z. Dang, M. Prato, R. Gaspari and L. Manna, *Chem. Mater.*, 2017, **29**, 7032–7041.

21 M. Rajabzadeh, R. Khalifeh, H. Eshghi and M. Bakavoli, *J. Catal.*, 2018, **360**, 261–269.

22 M. Sankar, N. Dimitratos, P. J. Miedziak, P. P. Wells, C. J. Kiely and G. J. Hutchings, *Chem. Soc. Rev.*, 2012, **41**, 8099.

23 S. De, J. Zhang, R. Luque and N. Yan, *Energy Environ. Sci.*, 2016, **9**, 3314–3347.

24 H. Naeimi and S. Mohammadi, *ChemistrySelect*, 2020, **5**, 2627–2633.

25 A. H. Ghasemi and H. Naeimi, *New J. Chem.*, 2020, **44**, 5056–5063.

26 H. Naeimi, A. Didar, Z. Rashid and Z. Zahraie, *J. Antibiot.*, 2017, **70**, 845.

27 A. Zare, A. Kohzadian, Z. Abshirini, S. S. Sajadikhah, J. Phipps, M. Benamara and M. H. Beyzavi, *New J. Chem.*, 2019, **43**, 2247–2257.

28 M. S. Mohamed, S. M. Awad and A. I. Sayed, *Molecules*, 2010, **15**, 1882–1890.

29 A. Zare, A. Kohzadian, H. Filian, M. S. G. Nezhad and A. Karami, *Res. Chem. Intermed.*, 2022, **48**, 1631–1644.

30 H. Naeimi and A. Didar, *J. Mol. Struct.*, 2017, **1137**, 626–633.

31 G. Zhang, H. Zhang, D. Yang, C. Li, Z. Peng and S. Zhang, *Catal. Sci. Technol.*, 2016, **6**, 6417–6430.

32 X. Han, W. Yan, K. Chen, C.-T. Hung, L.-L. Liu, P.-H. Wu, S.-J. Huang and S.-B. Liu, *Appl. Catal., A*, 2014, **485**, 149–156.

33 A. H. Ghasemi, A. Farazin, M. Mohammadimehr and H. Naeimi, *Mater. Today Commun.*, 2022, **31**, 103513.

34 A. Farazin, M. Mohammadimehr, A. H. Ghasemi and H. Naeimi, *RSC Adv.*, 2021, **11**, 32775–32791.

35 H. Naeimi and A. Didar, *Ultrason. Sonochem.*, 2017, **34**, 889–895.

36 H. Naeimi, A. Didar and Z. Rashid, *J. Iran. Chem. Soc.*, 2017, **14**, 377–385.